A Flux Model-Driven Transverse-Oriented Growth Strategy for the Synthesis of Large-Area Two-Dimensional Molybdenum-Based Materials

Citation for the original published paper (version of record):
Yan, C., Deng, L., Xu, S. et al (2025). A Flux Model-Driven Transverse-Oriented Growth Strategy for the Synthesis of Large-Area
Two-Dimensional Molybdenum-Based Materials. ACS Sustainable Chemistry & Engineering, 13(23): 8567-8579. http://dx.doi.org/10.1021/acssuschemeng.5c00325

ACS Sustainable Chemistry & Engineering
pubs.acs.org/journal/ascecg
Research Article

A Flux Model-Driven Transverse-Oriented Growth Strategy for the Synthesis of Large-Area Two-Dimensional Molybdenum-Based Materials

Caihong Yan, Liying Deng,* Shike Xu, Yang Li, Weiwei Jiang, Yijian Zhou, Jie Sun,* Xinghui Wang,* Zhong-Zhen Luo,* and Qun Yan

Cite This: *ACS Sustainable Chem. Eng.* 2025, 13, 8567−8579

Read Online

ACCESS | Metrics & More | Article Recommendations | Supporting Information

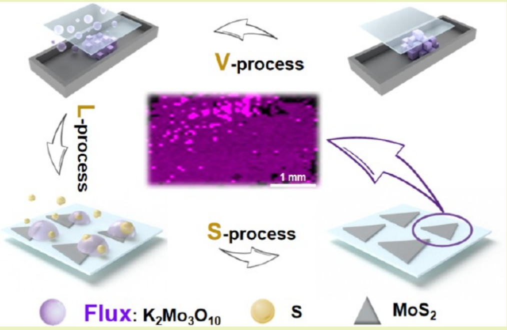

ABSTRACT: Mechanical exfoliation of thin sheets remains a prevalent technique for acquiring high-quality two-dimensional (2D) materials, as the chemical vapor deposition (CVD) technique for 2D transition metal dichalcogenides (TMDs) compounds lacks unambiguous theoretical guidance, complicating the precise control of material growth and the synthesis of the desired area and mass. In this paper, we establish the theoretical foundation of the vapor−liquid−solid (VLS) in CVD method growth of TMDs, i.e., the flux model, supported by theoretical analysis and experimental data. Utilizing this theoretical insight, this study proposes a nonvolatile molten salt flux-dominated VLS growth strategy. The introduction of potassium trimolybdate ($K_2Mo_3O_{10}$) as a stable molten salt medium enabled the cross-system controlled synthesis of molybdenum-based compounds (MoS_2, $MoSe_2$, MoO_2, Mo_3Te_4) by overcoming the reliance of the traditional VLS approach on volatile precursors. The low volatility of this molten salt flux and the synergistic diffusion effect of alkali metals markedly reduced nucleation density and facilitated the targeted lateral growth of atoms, resulting in the successful preparation of millimeter-sized single crystals (maximum size of 918 μm) and centimeter-sized continuous films. The MoS_2 films from this demonstrate exceptional electrical performance (mobility 21.74 $cm^2\ V^{-1}\ s^{-1}$, switching ratio ~10^5) in back-gated field-effect transistors with enhanced process compatibility. This study introduces a novel approach for the controllable synthesis of 2D semiconductors using molten salt flux engineering, with its cross-material applicability and centimeter-scale production capabilities establishing a basis for the sustainable manufacturing of wafer-scale electronic devices.

KEYWORDS: *molten salt assisted CVD, molybdenum disulfide, nucleation kinetics, nonvolatile flux, high quality, large size*

■ INTRODUCTION

Two-dimensional transition metal dichalcogenide (TMDs), characterized by atomic-level thickness, exhibit the potential for overcoming the size constraints of traditional silicon transistors among postsilicon electronic materials.[1−4] Molybdenum-based two-dimensional (2D) materials are particularly promising for nanoelectronic devices because of their exceptional electronic and optical characteristics.[5−7] Nonetheless, the fabrication of extensive and high-quality 2D molybdenum-based materials using chemical vapor deposition (CVD) continues to encounter several obstacles. First, the intricacy of the existing CVD reaction process for TMDs synthesis constrains the accurate management of the experimental procedure to a certain degree. Second, achieving precise control over nucleation density is challenging, as material growth predominantly depends on manipulating precursor vapor pressure. Third, the area of substrate-based epitaxial growth requires further development to satisfy commercial standards.

At this stage, actually, even the growth model of 2D molybdenum-based materials remains nascent and requires extensive exploration, not to mention the experimental obstacles involved. Currently, the growth promoters utilized in the CVD process, which is highly significant for manufacturing TMDs, predominantly consist of alkali metal halides.[8−12] Recent work indicates that the use of alkali metal halides to assist the growth of TMDs involves two reaction pathways: vapor−solid−solid (VSS) reactions involving halogens and vapor−liquid−solid (VLS) reactions involving alkali metals.[13−18] However, the VSS reaction pathway relies on vapor-phase transport activities, complicating the management of the reaction.[19] Further, Li et al. employed an alkali

Received: January 12, 2025
Revised: May 20, 2025
Accepted: May 21, 2025
Published: June 3, 2025

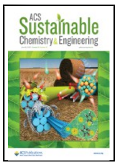

https://doi.org/10.1021/acssuschemeng.5c00325

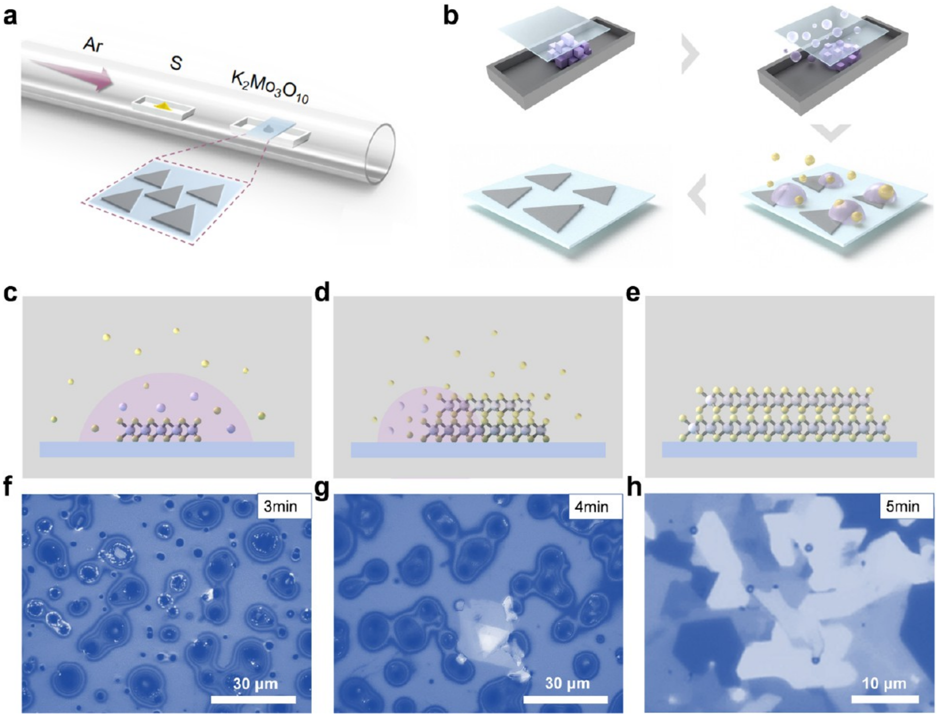

Figure 1. Growth of layered MoS_2 films by CVD. (a) Schematic diagram of the synthesis process of MoS_2 in the single-temperature zone CVD system. (b) Schematic diagram of the VLS process for transverse growth of MoS_2. (c−e) Schematic representation of the growth behavior of MoS_2 guided by the flux model. (f−h) Optical microscope images of MoS_2 growth for 3, 4, and 5 min.

metal-assisted CVD technique that only utilizes the VLS reaction pathway, hence streamlining the crystallization mechanism.[20] Regrettably, substantial research has focused on demonstrating that the growth mechanism of the alkali metal-assisted CVD approach occurs via the VLS process.[21−24] Specific theoretical models explaining the VLS growth mechanism are still missing. The formulation of growth theories elucidates experimental findings and subsequently enhances growth. Consequently, a comprehensive theoretical model that thoroughly elucidates the VLS synthesis of 2D molybdenum-based crystals and its associated variables is urgently necessary.

In this work, we first experimentally elucidate the theory underlying the VLS formation process, namely the flux model, a widely employed technique for synthesizing bulk single crystals. Informed by this previously established theory, we devised a targeted transverse-oriented growth strategy for the successful cross-system synthesis of millimeter-scale single crystals and layered nonlaminated molybdenum-based materials. The nonvolatile molybdate molten salt ($K_2Mo_3O_{10}$) does not readily form supersaturated solutions, hence diminishing nucleation.[25,26] The incorporation of alkali metals into the molten salt lessens the diffusion barrier.[27] Our methodology inhibits nucleation and favors epitaxial growth, thereby directing the atoms in the molten salt to develop through directional lateral diffusion. Raman spectroscopy verifies that the synthesized MoS_2 attains centimeter dimensions. Furthermore, the MoS_2 field-effect transistor exhibited exceptional characteristics, with carrier mobility attaining ~21.74 $cm^2\ V^{-1}\ s^{-1}$ and a switching ratio approaching ~10^5. This study elevates the VLS mechanism from an empirical process to a theory-guided universal approach through molten salt solvent engineering, providing a new material foundation for two-dimensional semiconductor wafer-level integration and sustainable electronics manufacturing.

■ RESULTS AND DISCUSSION

Validation of Theoretical Frameworks in Vapor−Liquid−Solid Growth. MoS_2 is a promising material for future electronic devices due to its distinctive electrical characteristics. Nonetheless, managing its growth remains a significant challenge. Consequently, we utilize MoS_2 as the primary example to demonstrate the flux model. The procedure for synthesizing MoS_2 on a commercially available sapphire substrate is detailed in Figure 1a and the Material and Methods section. At air pressure, $K_2Mo_3O_{10}$, sulfur powder, and substrate are sequentially placed into the tube furnace. The tube boiler was then subjected to a controlled temperature rise in an argon environment. After a 30 min reaction at 950 °C, the system was permitted to cool naturally to ambient temperature. The diagram of the detailed preparation device is shown in Figure S1. The placement of $K_2Mo_3O_{10}$, sulfur powder, and substrate in the tube furnace is shown in Figure S2. Figure 1b illustrates the development process of VLS MoS_2. First, the substrate was positioned on the $K_2Mo_3O_{10}$ powder before heating the reaction. As the temperature progressively approached the melting point of $K_2Mo_3O_{10}$ (~580 °C), the powder commenced melting.[26] As the temperature increases, molten $K_2Mo_3O_{10}$ begins to volatilize into many droplets (V-process). Concurrently, certain droplets travel downstream within the pipe containing the flowing argon gas, while some adhere to the sapphire substrate positioned above the powder. Subsequently, the sulfur powder liquefies and vaporizes into sulfur molecules upstream of the pipeline. A portion of the sulfur molecules was absorbed by the $K_2Mo_3O_{10}$ droplets on the substrate (L-process). The molybdenum and sulfur sources react in droplet form,

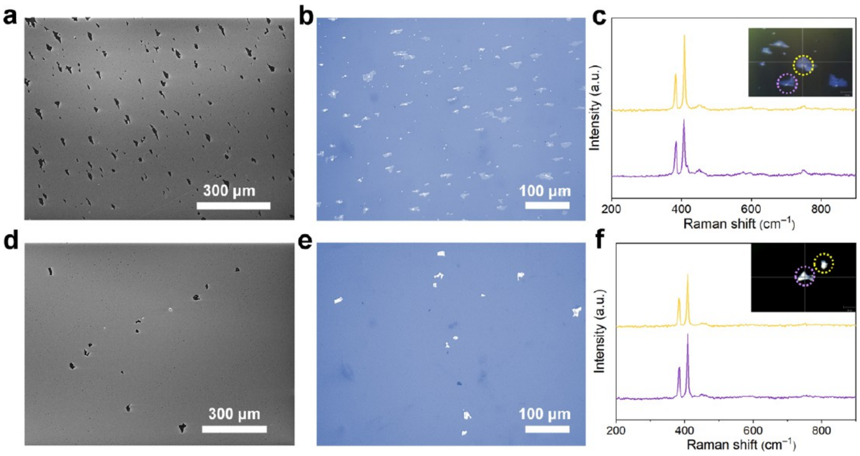

Figure 2. MoS_2 synthesized at different cooling rates. MoS_2 at a cooling rate of 15 °C/min: (a) SEM image. (b) Optical microscope image. (c) Raman spectrum. MoS_2 synthesized at a cooling rate of 10 °C/min: (d) SEM image. (e) Optical microscope image. (f) Raman spectrum.

nucleate, and grow on the sapphire substrate at increasing temperatures. Following a 30 min reaction at elevated temperature, byproducts and surplus sources of molybdenum and sulfur are completely volatilized. The substrate ends up with only a clean MoS_2 film (S-process).

The elucidation of the generalized theoretical mechanism of the VLS growth process primarily involves the modification of the reaction's growth duration. The duration of growth can control the growth process of MoS_2. Figure 1c−e illustrates the atomic framework of the nucleation and growth mechanism of MoS_2, encompassing melting and nucleation (stage 1), lateral growth (stage 2), and the development of two-dimensional flakes (stage 3). The optical microscope (OM) images in Figure 1f−h were acquired following quick cooling after exposure to elevated temperatures for 3, 4, and 5 min, respectively. In stage 1, sulfur powder and potassium trimolybdate liquefy above their melting point and vaporize onto the target substrate. As growth advances, MoS_2 initiates nucleation and crystallization. It appears as a translucent crystal near the droplet's center, as depicted in Figures S3a and 1f. Figures S3b and 1g illustrate the considerable lateral expansion of MoS_2 when maintained at elevated temperatures for 4 min (second stage). Two-dimensional MoS_2 lamellar crystals manifest near the center of the droplets on the substrate. The elevated temperature was sustained for 5 min before cooling; most of the flux dissipated, and the MoS_2 remained on the substrate postgrowth (third stage). Solvent residues are detectable at the peripheries of the 2D crystals (Figures S3c and 1h). Figure S3d presents an enhanced view of the residual flux in the third stage, illustrating that the flux surrounding the MoS_2 flake is distinctly circular, thereby confirming its existence in liquid form.[22] Furthermore, upon initiating lamellar epitaxy, the droplet size reaches several tens of micrometers within the first 3 min of the reaction. After 5 min of reaction, the droplet size had diminished by an order of magnitude, signifying that the growth driver (i.e., supersaturation) resulted from solvent evaporation. Figure 1 presents experimental evidence for the molten salt-assisted chemical vapor deposition reaction mechanism, the regulated lateral expansion of MoS_2 indicates crystal formation from the flux at elevated temperatures. The flux model's definition indicates that the resultant two-dimensional crystal (S) is the solute. The alkali metal molten salt (L) serves as the flux.[28]

The reaction's cooling rate was modified to confirm that the nucleation density of MoS_2 may be diminished by regulating the solvent's supersaturation. An increased cooling rate of the reaction results in a rapid decrease in the solubility of the solute inside the molten solution. The solution thus generates increased supersaturation, resulting in a corresponding alteration in the nucleation drive. This effect may render solution concentrations beyond the mesostable area more prone to nucleation.[29] The procedure states that following a 30 min reaction at 950 °C, the CVD system can naturally drop to ambient temperature. The cooling speeds of the CVD system were programmed at 15 °C/min and 10 °C/min to assess their impact on nucleation density. Figure 2a,b shows the scanning electron microscopy (SEM) and OM photographs of molybdenum disulfide at a 15 °C/min cooling rate, respectively. Figure 2d,e illustrates SEM and optical microscope pictures of MoS_2 at a heating rate of 10 °C/min. The typical peaks in the Raman spectra depicted in Figure 2c,f confirm that the 2D crystals on the substrate are both MoS_2. Figure 2 depicts that the density of MoS_2 single crystals at a cooling rate of 15 °C/min is markedly higher than that at a cooling rate of 10 °C/min, as evidenced by both SEM and OM images. At a cooling rate of 15 °C/min, the solubility of solutes in the molten liquid diminishes more swiftly than at a cooling rate of 10 °C/min. The level of supersaturation increases, resulting in an accelerated crystal precipitation rate and greater nuclei production. This occurrence confirms that the nucleation density of precipitated MoS_2 can be significantly diminished through flux conditioning. Consequently, the two-dimensional crystals' VLS process is essentially the flux model. In summary, elucidating the growth theory of the VLS process for 2D crystals establishes a definitive criterion to anticipate and direct 2D growth, encompassing the material's intrinsic features and the influence of external growth conditions. The primary growth factors are elucidated, offering robust guidelines for effectively regulating the experiment.

The precise regulation of the number of molybdenum disulfide layers was achieved by adjusting the spacing between the molybdenum source and the substrate (5−12 cm), combining the VLS flux model with the unique effect of the molten salt solvent. The flux of molybdenum source volatilized onto the substrate is significantly increased at short spacing (5 cm), leading to a high coverage of precursors on the substrate surface and an increase in the density of nucleation sites. The

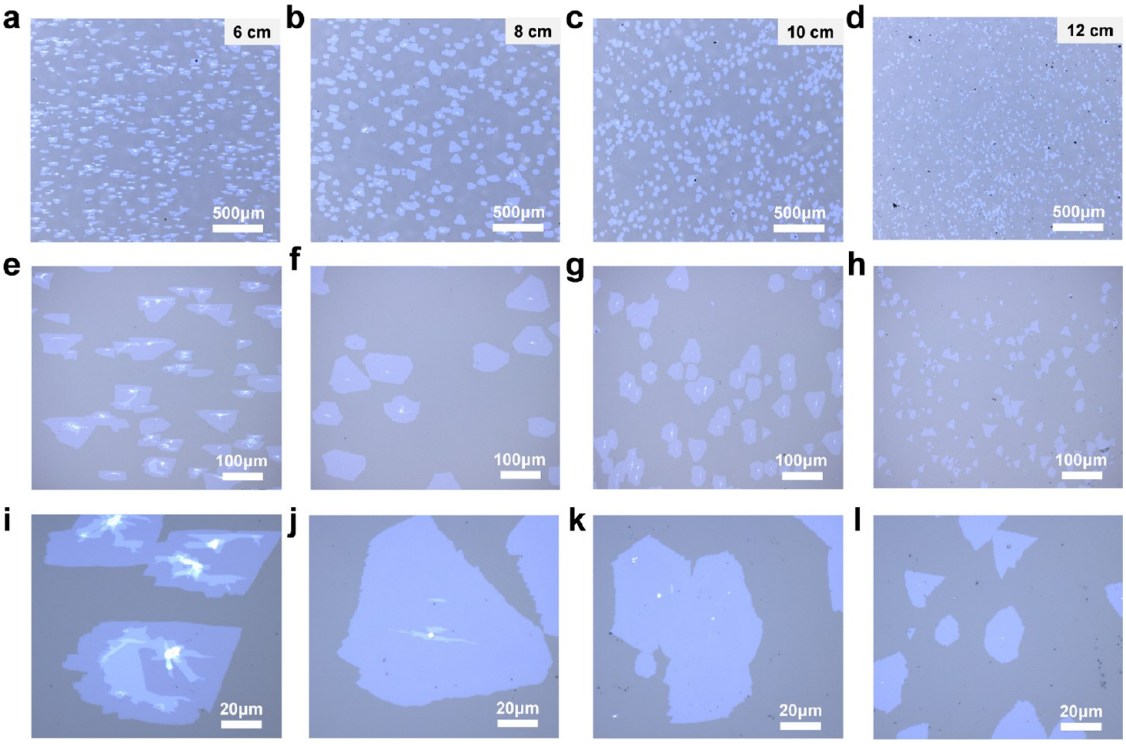

Figure 3. Modulation of the number of MoS_2 layers. Spacing between molybdenum source and substrate for synthesizing MoS_2: (a,e,i) 6 cm; (b,f,j) 8 cm; (c,g,k) 10 cm; (d,h,l) 12 cm.

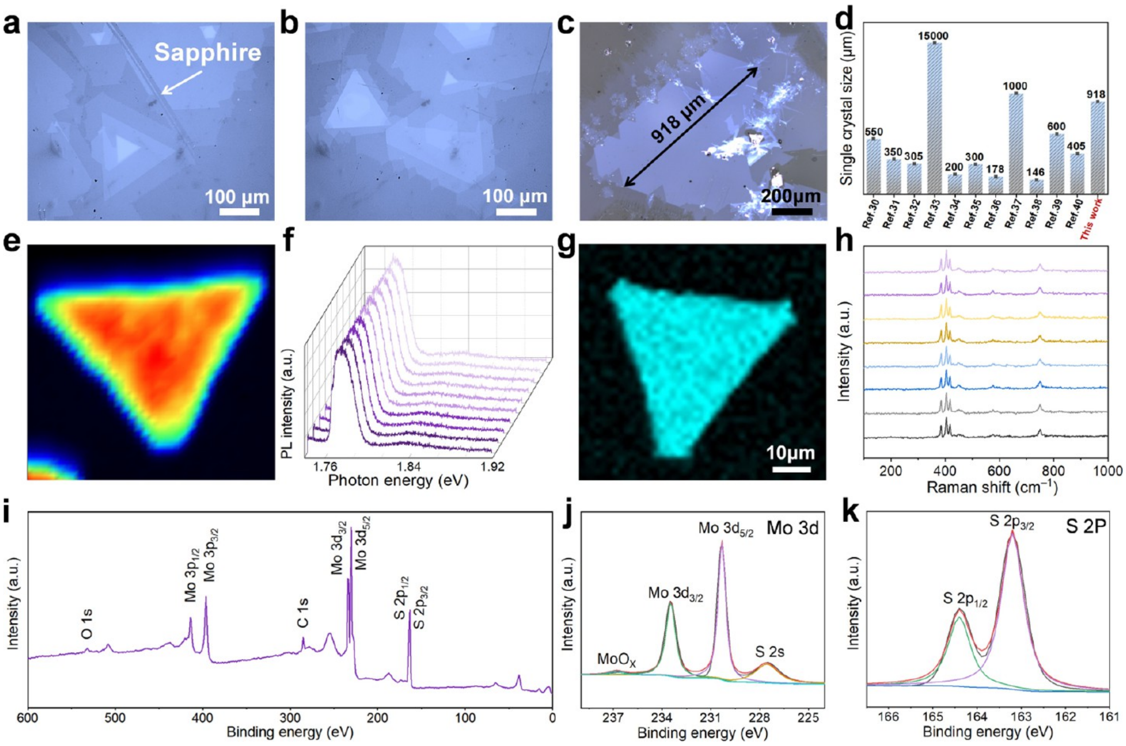

Figure 4. Optical and structural characterization of MoS_2. (a−c) Optical images of MoS_2 single crystals. (d) Plot of MoS_2 single crystal dimensions compared to recent literature. (e) Photoluminescence mapping of MoS_2. (f) Photoluminescence spectral images of MoS_2. (g) Raman mapping of the peaks at 385.71 cm^{-1}. (h) Raman spectral images of MoS_2. (i) XPS full spectrum of MoS_2 thin films. (j,k) XPS fine spectra of MoS_2 thin films.

adjacent crystal domains are vertically stacked due to the restricted diffusion space, forming a continuous multilayer film, as shown in Figure S4. As the spacing increases to 6−8 cm, the flux decreases, causing the nucleation density to decrease. The crystalline domains gain sufficient space for lateral diffusion and exhibit either a bilayer-dominated structure or a monolayer/bilayer hybrid state, as shown in Figure 3a,e,i,b,f,j. When the spacing is extended to 10−12 cm, the monolayer

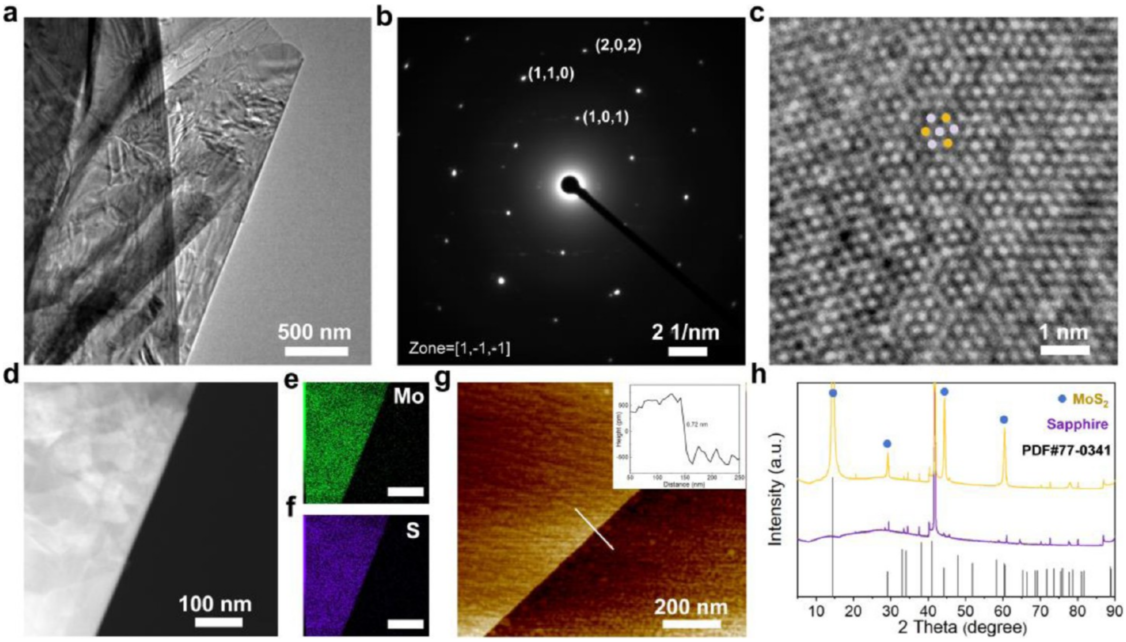

Figure 5. Structural characterization of MoS_2 single crystals. (a) Low magnification TEM image of MoS_2 transferred onto a TEM grid. (b) SAED pattern of MoS_2. (c) High magnification TEM image of MoS_2. (d−f) Elemental mapping of MoS_2 showing Mo and S distributions. (g) Typical AFM image of MoS_2. (h) XRD image of MoS_2 and substrate.

accounts for more than 95% (Figure 3c,g,k,d,h,l). This phenomenon stems from the dual function of the molten salt solvent (potassium trimolybdate): its nonvolatile character maintains a stable liquid-phase interface and promotes sulfur vapor dissolution and local supersaturation. Meanwhile, K^+ ions in the flux preferentially drive in-plane diffusion rather than vertical stacking. The K−Mo−O molten salt droplets formed by the $K_2Mo_3O_{10}$ precursor at high temperatures essentially constitute a typical VLS growth mode, fundamentally different from the conventional VSS growth. The irregular morphology of MoS_2 edges, as shown in Figure 3, directly manifests the kinetic anisotropy mediated by the liquid intermediate phase during the VLS growth process.[18] The liquid intermediate phase significantly reduces the nucleation energy barrier at the sulfur-terminated (S-terminated) edge by dissolving sulfur vapor and mediating Mo−S bonding reactions.[27] Thus, a lateral driving force is formed on the sapphire substrate with the sulfur end as the dominant growth direction, which makes the MoS_2 edges show fractal characteristics on the macroscopic scale. This phenomenon laterally verifies the synthesis of molybdenum disulfide using $K_2Mo_3O_{10}$ as a VLS process. Compared with conventional CVD, the present method demonstrates excellent process controllability by regulating the number of layers through a single parameter (spacing) without requiring complex carrier gas flow rate optimization.

A Flux Model-Driven Large-Scale Synthesis of MoS_2. The controlled synthesis of large-area MoS_2 is essential for next-generation electronics; thus, a targeted lateral growth technique is employed to achieve the production of large-sized MoS_2. To examine the surface morphology of MoS_2 thin films synthesized using the CVD process utilizing OM and SEM. Figure 4a,b presents optical microscope views of representative MoS_2 films. A noticeable scratch on the MoS_2 film is produced with tweezers, as depicted in Figure 4a. The darker sapphire substrate is visible beneath the scratches. At the same time, the remainder consists of a crystal of MoS_2. Triangular single-crystal MoS_2 with a millimeter scale was successfully prepared by systematic modulation. As shown in Figure 4c, the single-crystal domain region with a maximum edge length of 918 μm can be observed using optical microscopic characterization. Its geometric dimensions exhibit a significant advantage over the recently reported 2D MoS_2 single-crystal growth system (Figure 4d).[30−40] Notably, this breakthrough stems from the use of customized $K_2Mo_3O_{10}$ fluxes, which achieves a directional enhancement of crystal anisotropy growth. Figure S5 display the magnified SEM images of specific single MoS_2 monocrystals. The surface of MoS_2 synthesized with $K_2Mo_3O_{10}$ as the molybdenum precursor, is remarkably pristine, as evidenced by the images.

The crystalline quality and homogeneity of synthesized MoS_2 were evaluated by room-temperature photoluminescence (PL) spectroscopy and a Raman surface scanning system. A 450 nm laser was used to characterize the PL mapping of MoS_2 flakes under ambient conditions. The experimental results show that the PL intensity and peak position distributions in different regions exhibit high spatial consistency (shown in Figure 4e), indicating that the samples have excellent homogeneity. In addition, PL spectra of monolayers were measured at room temperature. The relevant selected single-crystal regions are located in Supporting Information Figure S6. As shown in Figure 4f, exhibit typical A-exciton emission peaks with a half-height width (fwhm) of ∼0.02 eV, which is in agreement with the PL characteristics of high-quality monolayers of MoS_2 reported in the literature.[41] Additionally, Raman mapping of MoS_2 on the sapphire substrate was conducted, focusing on the distinctive peaks of MoS_2 (385.71 cm^{-1}, 404.60 cm^{-1}).[42] The correlation microscope image of the Raman mapping is located in Figure S7a. Raman surface scans (Figures 4g and S7a,b) further show that the spatial intensity distributions of the E^1_{2g} (385.71 cm^{-1}) and A_{1g} (404.60 cm^{-1}) modes exhibit a highly consistent color contrast.[43,44] The peak spacings of the eight randomly selected regions are all 18.89 cm^{-1} in Figure 4h (single-layer feature).

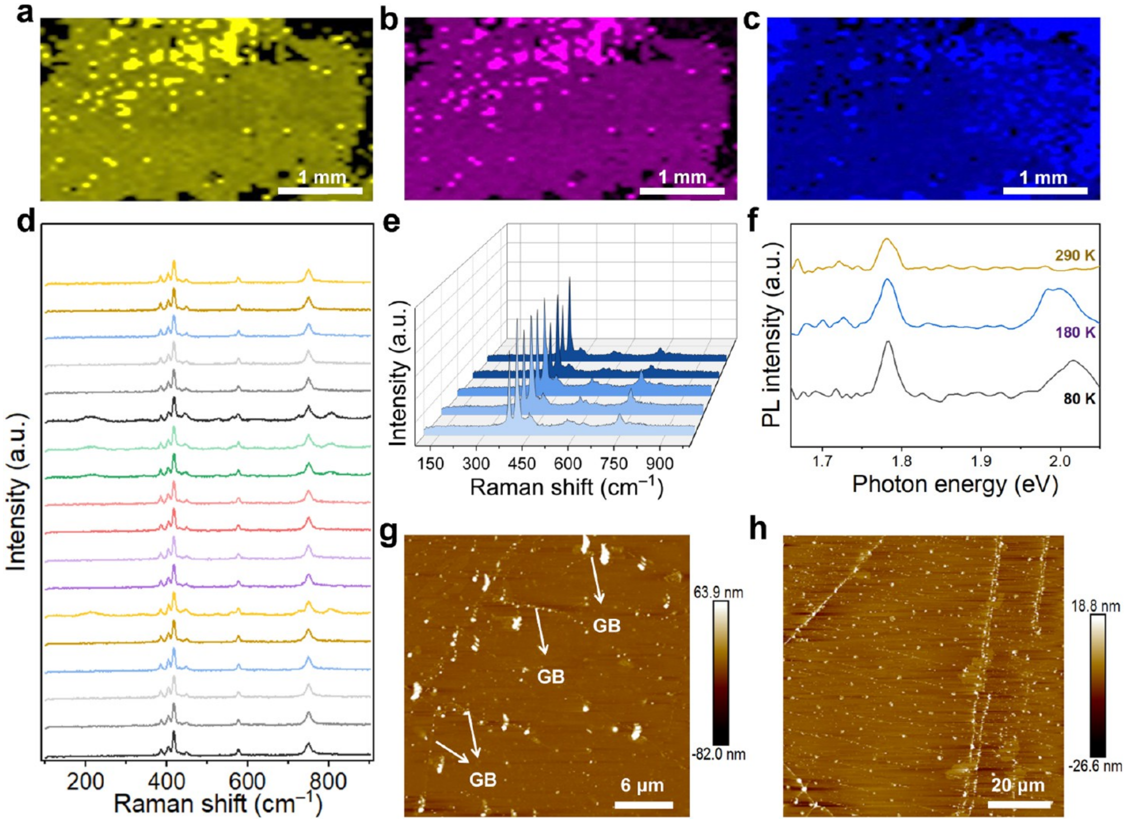

Figure 6. Surface and uniformity characterization of MoS_2 films: (a−c) Raman spectroscopy maps of the peaks at 404.7 cm^{-1}, 385.0 cm^{-1}, and substrate, respectively. (d) Random Raman spectra of the darker region of MoS_2 thin film. (e) Random Raman spectra of the brighter region of MoS_2 thin film. (f) PL spectra of MoS_2 films at low temperatures. (g,h) Typical AFM image of MoS_2 thin films.

Combined with the Raman pseudocolor map analysis of the supporting infographics Figure S7c,d, the MoS_2 films exhibit a uniform layer distribution. The above multiscale correlation between PL and Raman data validates the molten salt VLS strategy's effectiveness in synthesizing high-quality 2D semiconductors.

The chemical state of the MoS_2 films was examined by X-ray photoelectron spectroscopy (XPS), specifically analyzing the forms of Mo and S present in the films. Figure 4i depicts the XPS results of MoS_2 films within the binding energy range of 0−600 eV. The many peaks observed in the picture correspond to the S 2p peaks ($2p_{1/2}$, $2p_{3/2}$) and the Mo 3d peaks ($3d_{3/2}$, $3d_{5/2}$) in the MoS_2 films.[45] The O 1s peak primarily originates from the sapphire substrate (Al_2O_3). The limited range of Mo and S elements in MoS_2 depicted in Figure 4j,k indicates that the Mo $3d_{3/2}$ and Mo $3d_{5/2}$ peaks are at 233.5 and 230.3 eV, respectively.[46] The S $2p_{1/2}$ and S $2p_{3/2}$ peaks are observed at 164.4 and 163.2 eV, respectively. The locations of these peaks align with previously documented MoS_2 crystals, indicating the development of MoS_2 crystals. The peak at 227.5 eV in Figure 4j corresponds to S 2s, whereas the peak at 236.8 eV results from the partial sulfidation of the molybdenum source (MoO_x).[47] The diminished signal produced by MoO_x signifies a reduced density of surface imperfections in the samples. Consequently, optical microscopy, scanning electron microscopy, Raman mapping, and XPS assessments revealed that the MoS_2 single crystals exhibited both substantial dimensions and commendable crystal quality.

Systematic characterization employing selected area electron diffraction (SAED), atomic force microscopy (AFM), and X-ray diffractometry (XRD) was conducted to confirm the single-crystal structure of MoS_2. The MoS_2 samples exhibited folding on the copper mesh due to a complex transfer process prior to testing (Figure 5a). The SAED pattern of MoS_2 in Figure 5b exhibits six sets of symmetric diffraction spots, which arise from the hexagonal lattice of MoS_2. The uniform alignment of the dots indicates the characteristics of the single crystal. The high-magnification transmission electron microscopy (TEM) images (Figure 5c) reveal the periodic arrangement of atoms in a flawless honeycomb lattice within the folded MoS_2 samples.[42,48,49] In accordance with the atomic arrangement depicted in Figure 5c, we demonstrate the kind of MoS_2 folding by atomic configurations illustrated in Figure S8. Moreover, the elemental mapping pictures verify that Mo and O are equally distributed within the MoS_2 samples, as illustrated in Figure 5d−f.[50,51]

Raman spectra of MoS_2 on the copper mesh were measured using a focused laser (532 nm) at different laser powers (Figure S9a). It was observed that in the laser power range (~12−250 μW), all Raman modes of MoS_2 shifted linearly to lower frequencies with increasing laser power, a situation that led to the heating of MoS_2. The slope of the linear curve in Figure S9b, which is the power coefficient (χ_P) of the suspended MoS_2 A_{1g} modes, shows a small χ_P value and, therefore, a low thermal resistance, indicating a high in-plane thermal conductivity of MoS_2.[52] The AFM imaging verified that the thickness of MoS_2 single crystals is 0.72 nm (Figure 5g), which aligns closely with prior research.[51,53,54] Moreover, the consistent color contrast in AFM imaging indicated that the surface of the molybdenum disulfide flakes was very clean,

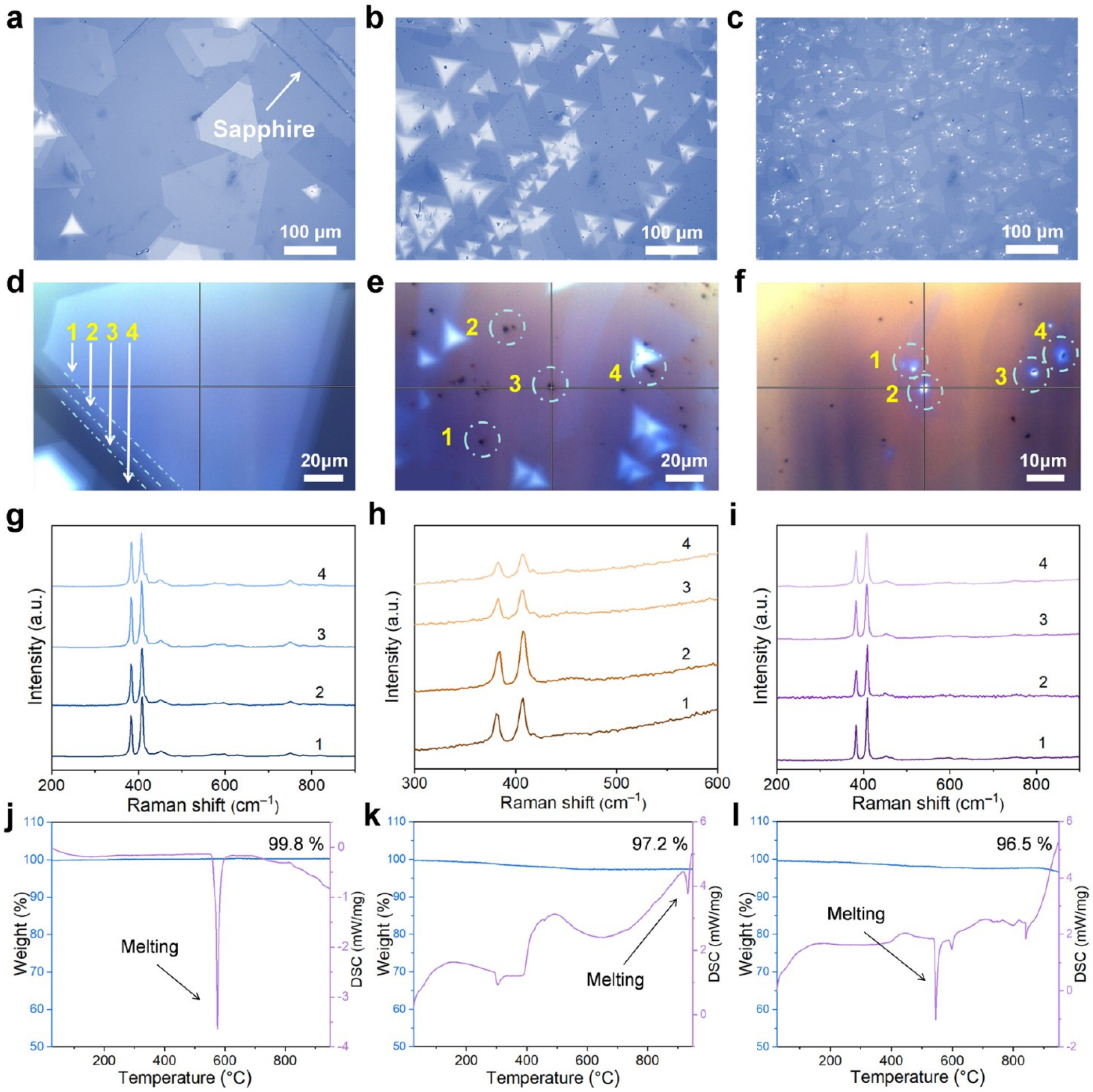

Figure 7. MoS_2 films prepared by different flux under the same conditions. Optical microscope images of prepared MoS_2: (a) $K_2Mo_3O_{10}$ as flux; (b) K_2MoO_4 as flux; (c) $K_2Mo_3O_{10}$:MoO_3 = 1:1 as flux. Raman images of prepared MoS_2: (d,g) $K_2Mo_3O_{10}$ as flux; (e,h) K_2MoO_4 as molybdenum source; (f,i) $K_2Mo_3O_{10}$:MoO_3 = 1:1 as flux. TG-DSC curves: (j) $K_2Mo_3O_{10}$; (k) K_2MoO_4; (l) $K_2Mo_3O_{10}$:MoO_3 = 1:1.

demonstrating that the synthesized MoS_2 single crystals exhibited high-quality attributes. The XRD test findings in Figure 5h indicate that the diffraction peaks of MoS_2 grown on sapphire are notably sharp, confirming the exceptional crystallinity of MoS_2 as demonstrated by TEM characterization.[55] Ultimately, TEM, elemental mapping, AFM, and XRD analyses of the synthesized molybdenum disulfide demonstrated that the produced MoS_2 exhibits superior crystal quality.

The structural homogeneity and grain boundary properties of centimeter-scale MoS_2 films were systematically evaluated by Raman surface scanning and AFM. Figure 6c shows the Raman mapping of the sapphire substrate, complementary to the mapping of the two characteristic peaks of molybdenum disulfide in Figure 6a,b. The figure illustrates that the dimensions of the synthesized MoS_2 films can attain a centimeter scale, further evidencing its superior thickness uniformity and commendable crystallinity across an extensive area. To clarify the homogeneity distribution, it was further analyzed by scanning dozens of randomly selected regions of the Raman surface, as shown in Figure 6d,e. The results show that the peak spacing $\Delta\omega$ between E^{1}_{2g} and A_{1g} peaks is stable at 18.9 cm^{-1} in the single-layer dominant region. At the same time, $\Delta\omega$ increases to 22–25 cm^{-1} in the localized highlight region, corresponding to the multilayer stacking. The multilayer stacked AFM image is shown in Figure S10a. Despite a few multilayer islands, their discrete distribution does not form penetrating defects. Figure 6f shows the PL spectra of the MoS_2 films from 290 K down to the lowest attainable temperature of 80 K. At low temperatures, any significantly larger line widths are dominated by the contribution of defect-induced inhomogeneities.[33] Only the more pronounced A-exciton peaks and B-exciton peaks are observed for molybdenum disulfide in Figure 6f. No emission peaks associated with defects are observed, and the half-peak width of the A exciton at 80 K is 20 meV, indicating a low defect density in the film.[56] The distribution of grain boundaries (GB) was identified by AFM (Figure 6g). By dividing the total length of the GB by the total counting area in Figure 6g, the density of the GB was measured to be 0.0957 μm^{-1}.[57] In

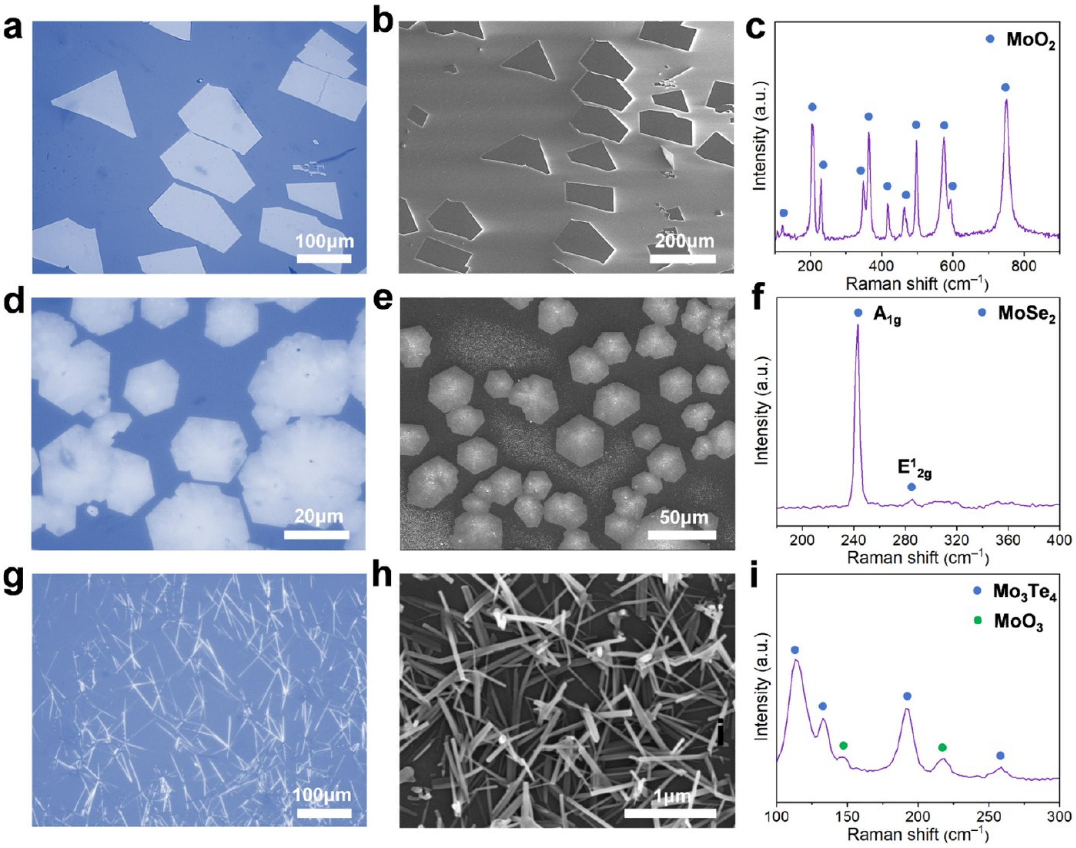

Figure 8. Morphology and chemical analysis of three other representative molybdenum-based materials. Optical microscope images of MoO_2 (a), $MoSe_2$ (d), and Mo_3Te_4 (g). SEM images of MoO_2 (b), $MoSe_2$ (e), and Mo_3Te_4 (h). Raman spectral images of MoO_2 (c), $MoSe_2$ (f), and Mo_3Te_4 (i).

addition, the surface characteristics of the films were systematically evaluated by wide-area AFM scanning (90 × 90 μm, the maximum field of view of the instrument) (Figures 6h and S10b), which showed that the sample surfaces exhibited a continuous and uniform morphology (roughness of 12.7 and 6.45 nm, respectively). Limited by the kinetic properties of the molten salt solvent-assisted growth, the films consist of single-crystal domains spliced together with a small number of highly mutated nanoparticles at the domain boundaries. The current data has demonstrated the feasibility and potential application of the molten salt solvent strategy in the synthesis of centimeter-scale 2D semiconductors.

Figure 7 compares three fluxes with varying volatilities to assess the suitability of potassium $K_2Mo_3O_{10}$, characterized by its reduced volatility, as a flux for producing MoS_2 films. Figure 7a illustrates the images of MoS_2 films synthesized from $K_2Mo_3O_{10}$. Figure 7a displays the substantial dimensions of the synthesized MoS_2 islands. The SEM pictures in Figure S11a,d illustrate that the MoS_2 surface is exceptionally clean, devoid of contaminants, and does not necessitate additional solvent treatment. As a comparison, Figure 7b depicts picture of MoS_2 films synthesized employing a flux (K_2MoO_4) that exhibits greater volatility than $K_2Mo_3O_{10}$, respectively.[58] Figure 7b reveals that the synthesized MoS_2 surface exhibits numerous tiny triangular MoS_2 single-crystal domains, signifying an elevated nucleation density of MoS_2 films produced using K_2MoO_4. The abundance of nucleation sites will not only come to limit the size of each MoS_2, but also introduce many grain boundaries. Excessive grain boundaries diminish the semiconductor's mobility by inducing carrier dispersion. Upon further magnification of the treatment utilizing SEM, several unidentified black compounds are observable on the surface of the MoS_2 film, as depicted in Figure S11b,e. This behavior suggests that the quality of MoS_2 films synthesized from K_2MoO_4 is suboptimal. Moreover, MoO_3, a prevalent molybdenum precursor for synthesizing MoS_2, has a greater saturation vapor pressure and, thus, increased volatility compared to $K_2Mo_3O_{10}$. MoS_2 films were synthesized by combining $K_2Mo_3O_{10}$ and MoO_3 in identical ratios and were compared to MoS_2 films derived from pure $K_2Mo_3O_{10}$. Figure 7c illustrates MoS_2 films synthesized with $K_2Mo_3O_{10}$:MoO_3 in a 1:1 ratio as the flux. At the equivalent magnification of Figure 7a,b, the optical image in Figure 7c displays a singular MoS_2 domain characterized by a diminutive size and numerous dense brilliant particles. The SEM magnification of the pictures indicated that these small particles predominantly occupied the middle of the MoS_2 islands and had a three-dimensional architecture (Figure S11c,f). These three-dimensional particles were previously documented in prior studies of MoS_2 films synthesized from MoO_3.[34] We speculate that these particles are nucleation sites of MoS_2.

Raman spectroscopy was employed to further assess the crystal quality of MoS_2 synthesized from various melts and identify unidentified compounds on the MoS_2 surface. Figure 7g presents the Raman spectra of MoS_2 synthesized from $K_2Mo_3O_{10}$, corresponding to the four areas marked by arrows in Figure 7d. The peaks at 407.4 cm^{-1} and 382.9 cm^{-1} in the figure are characteristic of layered MoS_2.[59] Figure 7h displays

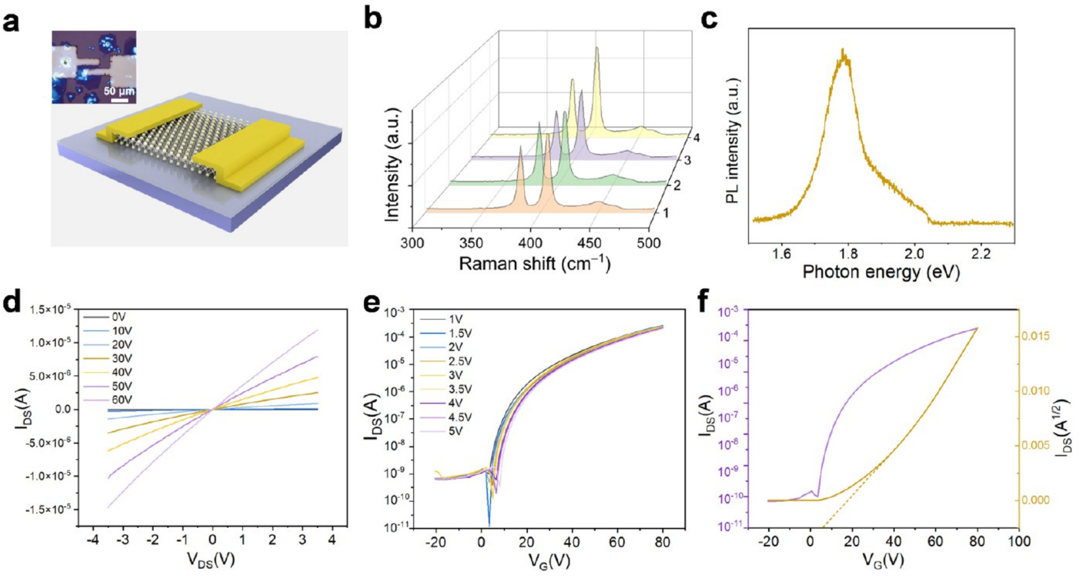

Figure 9. Electrical characteristics of MoS_2 derived from $K_2Mo_3O_{10}$ precursor. (a) Diagram of MoS_2 field-effect transistor. The inset shows an optical image of the device. (b) Raman spectra of MoS_2 in the channel. (c) PL spectra of MoS_2 in the channel. (d) Characteristics of the gadget pertaining to $I_{DS}-V_{DS}$. (e) Transmission characteristics of the device at varying V_{DS}. (f) Transmission characteristics with a constant drain-source bias of V_{DS} = 1 V.

the Raman spectra of the black substance observed on the surface of MoS_2 films synthesized with K_2MoO_4, corresponding to the four areas shown in Figure 7e. The Raman spectra of these black compounds exhibit distinctive peaks of MoS_2. The utilization of K_2MoO_4 for the synthesis of MoS_2 films is suboptimal. Figure 7i illustrates the Raman spectra of three-dimensional particles present on the surface of MoS_2 films synthesized using $K_2Mo_3O_{10}$:MoO_3 = 1:1 as flux, corresponding to the four locations highlighted in Figure 7f. The Raman spectra of these three-dimensional particles exhibit distinctive peaks of MoS_2, confirming our hypothesis that they serve as nucleation sites for MoS_2. In addition, thermogravimetric analyses of $K_2Mo_3O_{10}$, K_2MoO_4, and $K_2Mo_3O_{10}$:MoO_3 = 1:1 were performed under an inert atmosphere (nitrogen) (temperature range of 25−950 °C, ramping rate of 15 °C/min). The mass loss curves were recorded in real-time using the synchrotron thermal analyzer STA 449 F5 of NETZSCH, Germany. Thermogravimetric analysis (TGA) experiments performed under simulated reaction conditions showed that $K_2Mo_3O_{10}$ exhibits significant low volatility characteristics compared to K_2MoO_4 and $K_2Mo_3O_{10}$:MoO_3 (1:1) mixtures. The mass retention of K_2MoO_4 was 97.2% due to pyrolysis and gas-phase volatilization in the range of 25−950 °C at a temperature increase rate of 15 °C/min. Differential scanning calorimetry (DSC) analysis showed that it melted at 920 °C, which followed the previous study, whereas $K_2Mo_3O_{10}$ lost only 0.2% of its mass in the same temperature region, indicating its higher thermal stability and low volatility. DSC showed that $K_2Mo_3O_{10}$ melted at 580 °C, which verified the previous judgment. For the $K_2Mo_3O_{10}$:MoO_3 mixture, the mass ultimately remained at 96.5% after heating from 25 to 950 °C, which was considered due to the sublimation of the MoO_3 resulting in mass loss. The low volatility allowed $K_2Mo_3O_{10}$ to maintain a stable supply of liquid-phase precursors during MoS_2 growth, avoiding nonuniform nucleation due to rapid depletion of the Mo source or localized supersaturation. Comparing the two prevalent fluxes employed in the synthesis of MoS_2 films with $K_2Mo_3O_{10}$ reveals that the MoS_2 films produced utilizing the more volatile K_2MoO_4 and MoO_3 exhibit dense nucleation sites, resulting in smaller MoS_2 single-crystal domains. The more volatile molten fluxes progressively evaporate from the liquid surface at elevated reaction temperatures. The solution reaches supersaturation more rapidly, facilitating excessive crystal nucleation driving forces. Consequently, the nonvolatile $K_2Mo_3O_{10}$ molten liquid is less prone to supersaturation than other fluxes. This finding confirms that nonvolatile solvents can significantly diminish the nucleation density of MoS_2 by lowering the driving force for crystal nucleation, illustrating that various fluxes can directly influence the formation of 2D crystals.

Versatile Synthesis of Molybdenum-Based Crystalline Materials. The flux model is also relevant for the synthesis of other TMDs materials. The nonvolatile flux $K_2Mo_3O_{10}$, obtained using the molten salt process in CVD, facilitates the synthesis of molybdenum-based materials with diverse compositions and physical characteristics. To this end, three additional prevalent molybdenum-based compounds (MoO_2, $MoSe_2$, and Mo_3Te_4) were synthesized utilizing a comparable methodology, as illustrated in Figure 8, highlighting the appropriateness of $K_2Mo_3O_{10}$. The synthesized MoO_2 exhibited irregular morphologies, as illustrated in Figure 8a,b. Various morphologies of MoO_2 crystals were examined utilizing Raman spectroscopy, as illustrated in Figures 8c and S12a−c. The Raman peaks of rectangular, triangular, and irregular pentagonal MoO_2 crystals, depicted in Figure 8a,b, are consistent. The positions of the peaks are 120.8 cm^{-1},206.5 cm^{-1}, 229.7 cm^{-1}, 348.4 cm^{-1}, 365.5 cm^{-1}, 418.4 cm^{-1}, 463.5 cm^{-1}, 497.2 cm^{-1}, 575.1 cm^{-1}, 591.7 cm^{-1}, and 750.3 cm^{-1}, which are in agreement with those previously reported for the MoO_2 crystals.[60] The elemental mapping diagrams further validated the homogeneous distribution of elements within the MoO_2 crystals, as depicted in Figure S13a−d. The synthesized $MoSe_2$ crystals are visible in the optical microscope and SEM pictures presented in Figure 8d,e. $MoSe_2$ crystals predominantly exhibit a hexagonal morphology, with the associated

Raman spectral data presented in Figure 8f. The peaks in the spectra at 243.1 cm^{-1} and 285.4 cm^{-1} correspond to typical $MoSe_2$ crystals.[61,62] The elemental mapping of $MoSe_2$ crystals, depicted in Figure S14, illustrates the consistent distribution of the Mo and Se elements. A comparable technique was employed to synthesize Mo_3Te_4. Figure 8g,h illustrates that the synthesized Mo_3Te_4 exhibits needle-shaped crystals. The positions of the peaks were determined using Raman testing to be at 113.5 cm^{-1}, 132.9 cm^{-1}, 146.6 cm^{-1}, 193.1 cm^{-1}, 218.4 cm^{-1}, and 258.9 cm^{-1}. The peaks at 146.6 cm^{-1} and 218.4 cm^{-1} correspond to the characteristic peaks of the byproduct MoO_3.[63] The remaining peaks are attributed to the characteristic peaks of Mo_3Te_4 (Figure 8i).[64] The EDS examination confirmed that the produced needle crystals are Mo_3Te_4, with an elemental ratio of Mo to Te of 0.78 (Figure S15). The atomic ratio closely aligns with the expected atomic ratio of Mo_3Te_4 (0.75), confirming that the needle crystals are identified as Mo_3Te_4. This event indicates that the $K_2Mo_3O_{10}$ solvent is appropriate for synthesizing many high-quality molybdenum-based crystalline minerals, including MoS_2, MoO_2, $MoSe_2$, and Mo_3Te_4.

Electrical Measurements of Field Effect Transistors. Figure 9a presents a three-dimensional schematic and optical representation of a conventional MoS_2 device for field-effect transistor measurements (inset). An enlarged view of the optical microscope image of the MoS_2 device is located in Figure S16a. MoS_2 was deposited on a 300 nm SiO_2/Si substrate with Ti/Al/Ti top contacts for the standard device. The device configuration facilitates the evaluation of three-terminal FETs utilizing Si (p++) as the back gate. For the channel length definition and layer number verification, it was confirmed by systematic Raman spectroscopy and PL spectroscopy analysis that the Raman characteristic peaks in the parallel region between the fork-finger electrodes in Figure 9a are located at 382.93 cm^{-1} and 405.6 cm^{-1}, as shown in Figure 9b. The corresponding Raman test points are shown in Figure S16b. The characteristic peak difference is 22.67 cm^{-1} (double layer), which significantly differs from the 24.56 cm^{-1} peak difference in the nonparallel region (the latter is consistent with the three-layer MoS_2 property). In addition, the sensitivity of the PL test to the number of layers decreases significantly in bilayer materials due to a shift in the exciton complexation mechanism (monolayer MoS_2 shows direct bandgap luminescence, whereas bilayers are indirectly bandgapped, leading to a decrease in PL intensity).[65−67] Lower PL spectral intensity of MoS_2 in the channel is observed in Figure 9c. Synergistic analysis of PL intensity decay with Raman vibrational mode shifts verifies the bilayer nature of MoS_2 in the channel region. Figure 9d illustrates the $I-V$ characteristics of a standard device with a channel length (L) of approximately 10 μm and a width (W) of roughly 40 μm. The linear and symmetrical output current−voltage characteristics ($I_{DS}-V_{DS}$) of the MoS_2 FETs, evaluated at ambient temperature, demonstrate ohmic behavior, suggesting that MoS_2 transistors with Ti/Al/Ti contacts possess comparatively low contact resistance.[68] Figure 9e illustrates the transmission curves under varying V_{DS} conditions. The I_{DS} values rise consistently with increasing V_G, demonstrating n-type behavior akin to previously reported devices.[69,70] Figure 9e illustrates a maximum on/off current ratio of approximately ~10^5 and a threshold voltage of roughly ~8 V (Figure 9f). Charge carrier mobility in FET devices is assessed by

$$\mu = \frac{L}{WC_{OX}V_{DS}}\frac{dI_{DS}}{dV_G} \tag{1}$$

The transport curves depicted in Figure 9f indicate that the mobility of MoS_2, achieved with optimal ohmic connections, was measured at ~ 21.74 $cm^2\ V^{-1}\ s^{-1}$. The carrier mobility is consistent with previously documented values, indicating that the high-quality MoS_2 thin films derived from the $K_2Mo_3O_{10}$ precursor demonstrate superior electrical properties.[68]

CONCLUSIONS

In summary, we emphasize that the VLS process utilizes flux model to obtain new understandings of the growth of 2D materials, serving as a reliable reference for experimental work. For example, the degree of supersaturation of the flux can influence the growth of 2D crystalline materials. In addition, the theoretical model applies to the VLS process in the molten salt-assisted CVD method, which is unconstrained by crystal structure and elemental composition and can be extended to both lamellar and nonlamellar materials (including oxides, sulfides, etc.), thereby enhancing the theoretical investigation and chemical synthesis of 2D materials.

Guided by flux model, we provide a targeted transverse-oriented growth strategy aimed at synthesizing several two-dimensional molybdenum-based materials, including layered MoS_2 and $MoSe_2$, as well as nonlayered MoO_2 and Mo_3Te_4, utilizing $K_2Mo_3O_{10}$ as a solvent. We employ the extent of solvent supersaturation to control the nucleation of molybdenum disulfide crystals to assess the applicability of flux model to the viability of the VLS reaction process. Importantly, scanning electron microscopy and Raman characterization revealed that larger sizes, reaching the centimeter scale, were achieved using $K_2Mo_3O_{10}$ as the flux. Ultimately, we present a MoS_2-based FET exhibiting commendable electrical performance. This study presents an alternate method for producing huge, high-quality 2D semiconductors.

ASSOCIATED CONTENT

Supporting Information

The Supporting Information is available free of charge at https://pubs.acs.org/doi/10.1021/acssuschemeng.5c00325.

Figure S1: The diagram of the detailed preparation device. Figure S2: The placement of $K_2Mo_3O_{10}$, sulfur powder, and substrate in the tube furnace. Figure S3: Solvent residues are detectable at the peripheries of the 2D crystals. Figure S4: The adjacent crystal domains are vertically stacked due to the restricted diffusion space, forming a continuous multilayer film. Figure S5: The magnified SEM images of specific single MoS_2 monocrystals. Figure S6: Optical microscope image during PL spectroscopy measurement. Figure S7: The correlation microscope image of the Raman mapping. Figure S8: The kind of MoS_2 folding by atomic configurations. Figure S9: Raman spectra of MoS_2 on the copper mesh were measured using a focused laser (532 nm) at different laser powers. Figure S10: The multilayer stacked AFM image. Figure S11: SEM images of molybdenum disulfide prepared from different molybdenum sources. Figure S12: Various morphologies of MoO_2 crystals were examined utilizing Raman spectroscopy. Figure S13: The elemental mapping diagrams further validated the homogeneous distribution of elements within the MoO_2 crystals. Figure S14: The elemental mapping of $MoSe_2$ crystals. Figure S15: The EDS examination confirmed that the produced needle crystals are Mo_3Te_4, with an elemental ratio of Mo to Te of 0.78. Figure S16: An enlarged view of the optical microscope image of the MoS_2 device (PDF)

AUTHOR INFORMATION

Corresponding Authors

Liying Deng − *Fujian Key Laboratory of Agricultural Information Sensing Technology, College of Mechanical and Electrical Engineering, Fujian Agriculture and Forestry University, Fuzhou 350002, China*; Email: dly@fafu.edu.cn

Jie Sun − *National and Local United Engineering Laboratory of Flat Panel Display Technology, Fujian Science & Technology Innovation Laboratory for Optoelectronic Information of China, Fuzhou University, Fuzhou 350100, China; Quantum Device Physics Laboratory, Department of Microtechnology and Nanoscience, Chalmers University of Technology, Gothenburg 41296, Sweden*; Email: jie.sun@fzu.edu.cn

Xinghui Wang − *National and Local United Engineering Laboratory of Flat Panel Display Technology, Fujian Science & Technology Innovation Laboratory for Optoelectronic Information of China, Fuzhou University, Fuzhou 350100, China*; orcid.org/0000-0002-5384-0666; Email: seaphy23@fzu.edu.cn

Zhong-Zhen Luo − *Key Laboratory of Advanced Materials Technologies, International (Hong Kong Macao and Taiwan) Joint Laboratory on Advanced Materials Technologies, College of Materials Science and Engineering, Fuzhou University, Fuzhou 350108, P. R. China*; orcid.org/0000-0003-4331-6286; Email: zzluo@fzu.edu.cn

Authors

Caihong Yan − *National and Local United Engineering Laboratory of Flat Panel Display Technology, Fujian Science & Technology Innovation Laboratory for Optoelectronic Information of China, Fuzhou University, Fuzhou 350100, China*; orcid.org/0009-0006-2569-7678

Shike Xu − *Key Laboratory of Advanced Materials Technologies, International (Hong Kong Macao and Taiwan) Joint Laboratory on Advanced Materials Technologies, College of Materials Science and Engineering, Fuzhou University, Fuzhou 350108, P. R. China*

Yang Li − *National and Local United Engineering Laboratory of Flat Panel Display Technology, Fujian Science & Technology Innovation Laboratory for Optoelectronic Information of China, Fuzhou University, Fuzhou 350100, China*

Weiwei Jiang − *State Key Laboratory for Modification of Chemical Fibers and Polymer Materials, College of Chemistry and Chemical Engineering, Donghua University, Shanghai 201620, P. R. China*

Yijian Zhou − *National and Local United Engineering Laboratory of Flat Panel Display Technology, Fujian Science & Technology Innovation Laboratory for Optoelectronic Information of China, Fuzhou University, Fuzhou 350100, China*

Qun Yan − *National and Local United Engineering Laboratory of Flat Panel Display Technology, Fujian Science & Technology Innovation Laboratory for Optoelectronic Information of China, Fuzhou University, Fuzhou 350100, China*

Complete contact information is available at:
https://pubs.acs.org/10.1021/acssuschemeng.5c00325

Notes

The authors declare no competing financial interest.

ACKNOWLEDGMENTS

We thank the support from National Key Research and Development Program of China (nos. 2023YFB3608703 and 2023YFB3608700), National Natural Science Foundation of China (no. 12474066), Fujian Science & Technology Innovation Laboratory for Optoelectronic Information of China (nos. 2021ZZ122 and 2020ZZ110), and Fujian provincial projects (nos. 2021HZ0114 and 2024J011312).

REFERENCES

(1) Hussain, S.; Zhou, R.; Li, Y.; Qian, Z.; Urooj, Z.; Younas, M.; Zhao, Z.; Zhang, Q.; Dong, W.; Wu, Y.; Zhu, X.; Wang, K.; Chen, Y.; Liu, L.; Xie, L. Liquid Phase Edge Epitaxy of Transition-Metal Dichalcogenide Monolayers. *J. Am. Chem. Soc.* **2023**, *145* (20), 11348−11355.

(2) Yin, L.; Cheng, R.; Ding, J.; Jiang, J.; Hou, Y.; Feng, X.; Wen, Y.; He, J. Two-Dimensional Semiconductors and Transistors for Future Integrated Circuits. *ACS Nano* **2024**, *18* (11), 7739−7768.

(3) Zhang, W.; Hao, H.; Lee, Y.; Zhao, Y.; Tong, L.; Kim, K.; Liu, N. One-Interlayer-Twisted Multilayer MoS_2 Moiré Superlattices. *Adv. Funct. Mater.* **2022**, *32* (19), 2111529.

(4) Zhao, T.; Guo, J.; Li, T.; Wang, Z.; Peng, M.; Zhong, F.; Chen, Y.; Yu, Y.; Xu, T.; Xie, R.; Gao, P.; Wang, X.; Hu, W. Substrate Engineering for Wafer-scale Two-dimensional Material Growth: Strategies, Mechanisms, and Perspectives. *Chem. Soc. Rev.* **2023**, *52* (5), 1650−1671.

(5) Kim, T. S.; Noh, G.; Kwon, S.; Kim, J. Y.; Dhakal, K. P.; Oh, S.; Chai, H.-J.; Park, E.; Kim, I. S.; Lee, E.; Kim, Y.; Lee, J.; Jo, M.-k.; Kang, M.; Park, C.; Kim, J.; Park, J.; Kim, S.; Kim, M.; Kim, Y.; Choi, S.-Y.; Song, S.; Jeong, H. Y.; Kim, J.; Kwak, J. Y.; Kang, K. Diffusion Control on the Van der Waals Surface of Monolayers for Uniform Bi-Layer MoS_2 Growth. *Adv. Funct. Mater.* **2024**, *34* (23), 2312365.

(6) Hu, J.; Zhou, F.; Wang, J.; Cui, F.; Quan, W.; Zhang, Y. Chemical Vapor Deposition Syntheses of Wafer-Scale 2D Transition Metal Dichalcogenide Films toward Next-Generation Integrated Circuits Related Applications. *Adv. Funct. Mater.* **2023**, *33* (40), 2303520.

(7) Li, L.; Wang, Q.; Wu, F.; Xu, Q.; Tian, J.; Huang, Z.; Wang, Q.; Zhao, X.; Zhang, Q.; Fan, Q.; Li, X.; Peng, Y.; Zhang, Y.; Ji, K.; Zhi, A.; Sun, H.; Zhu, M.; Zhu, J.; Lu, N.; Lu, Y.; Wang, S.; Bai, X.; Xu, Y.; Yang, W.; Li, N.; Shi, D.; Xian, L.; Liu, K.; Du, L.; Zhang, G. Epitaxy of Wafer-scale Single-crystal MoS_2 Monolayer via Buffer Layer Control. *Nat. Commun.* **2024**, *15* (1), 1825.

(8) Kim, M.; Son, M.; Seo, D.-B.; Kim, J.; Jang, M.; Kim, D. I.; Lee, S.; Yim, S.; Song, W.; Myung, S.; Yoo, J.-W.; Lee, S. S.; An, K.-S. Dual Catalytic and Self-Assembled Growth of Two-Dimensional Transition Metal Dichalcogenides Through Simultaneous Predeposition Process. *Small* **2023**, *19* (22), 2206350.

(9) Shi, B.; Zhou, D.; Qiu, R.; Bahri, M.; Kong, X.; Zhao, H.; Tlili, C.; Wang, D. High-efficiency Synthesis of Large-area Monolayer WS_2 Crystals on SiO_2/Si Substrate via NaCl-assisted Atmospheric Pressure Chemical Vapor Deposition. *Appl. Surf. Sci.* **2020**, *533*, 147479.

(10) Chang, Y.-P.; Li, W.-B.; Yang, Y.-C.; Lu, H.-L.; Lin, M.-F.; Chiu, P.-W.; Lin, K.-I. Oxidation and Degradation of WS_2 Monolayers Grown by NaCl-Assisted Chemical Vapor Deposition: Mechanism and Prevention. *Nanoscale* **2021**, *13* (39), 16629−16640.

(11) Singh, A.; Moun, M.; Sharma, M.; Barman, A.; Kumar Kapoor, A.; Singh, R. NaCl-assisted Substrate Dependent 2D Planar Nucleated Growth of MoS_2. *Appl. Surf. Sci.* **2021**, *538*, 148201.

(12) Wibowo, A. A.; Tebyetekerwa, M.; Bui, A. D.; Truong, T. N.; Saji, S.; Kremer, F.; Yang, Z.; Yin, Z.; Lu, Y.; Macdonald, D.; Nguyen, H. T. Hybrid Alkali Salt Catalysts-Promoted CVD Growth of 2D $MoSe_2$−WSe_2 and WSe_2−$MoSe_2$ Lateral Heterostructures. *Adv. Mater. Technol.* **2023**, *8* (15), 2300143.

(13) Li, S. Salt-assisted Chemical Vapor Deposition of Two-dimensional Transition Metal Dichalcogenides. *iScience* **2021**, *24* (11), 103229.

(14) Tian, C.; Xiao, R.; Sui, Y.; Feng, Y.; Wang, H.; Zhao, S.; Liu, J.; Gao, X.; Sun, H.; Peng, S.; Jin, Z.; Liu, X.; Wang, S.; Li, P.; Yu, G. Opposite Doping Distribution in TMD Monolayer Regulated by VLS and VSS Growth Mechanism. *Sci. China Mater.* **2023**, *66* (12), 4723−4732.

(15) Yu, C.; Chang, P.; Guan, L.; Tao, J. Inward Growth of Monolayer MoS_2 Single Crystals from Molten Na_2MoO_4 Droplets. *Mater. Chem. Phys.* **2020**, *240*, 122203.

(16) Li, S.; Lin, Y.-C.; Liu, X.-Y.; Hu, Z.; Wu, J.; Nakajima, H.; Liu, S.; Okazaki, T.; Chen, W.; Minari, T.; Sakuma, Y.; Tsukagoshi, K.; Suenaga, K.; Taniguchi, T.; Osada, M. Wafer-scale and Deterministic Patterned Growth of Monolayer MoS_2 via Vapor−liquid−solid Method. *Nanoscale* **2019**, *11* (34), 16122−16129.

(17) Baheri, Y. T.; Hedayati, M. A.; Maleki, M.; Karimian, H. A Vapor-liquid-solid Mechanism for In-situ Deposition of Ultra-small Hollow MoS_2 Nanoparticles in N-doped carbon foam as an anode of lithium-ion batteries. *J. Energy Storage* **2023**, *68*, 107682.

(18) Li, S.; Lin, Y.-C.; Zhao, W.; Wu, J.; Wang, Z.; Hu, Z.; Shen, Y.; Tang, D.-M.; Wang, J.; Zhang, Q.; Zhu, H.; Chu, L.; Zhao, W.; Liu, C.; Sun, Z.; Taniguchi, T.; Osada, M.; Chen, W.; Xu, Q.-H.; Wee, A. T. S.; Suenaga, K.; Ding, F.; Eda, G. Vapour−liquid−solid Growth of Monolayer MoS_2 Nanoribbons. *Nat. Mater.* **2018**, *17* (6), 535−542.

(19) Kim, H.; Yoo, Y. Confined Fluxes Mediate 2D Growth. *Nat. Synth.* **2022**, *1* (11), 833−834.

(20) Li, S.; Lin, Y.-C.; Hong, J.; Gao, B.; Lim, H. E.; Yang, X.; Liu, S.; Tateyama, Y.; Tsukagoshi, K.; Sakuma, Y.; Suenaga, K.; Taniguchi, T. Mixed-Salt Enhanced Chemical Vapor Deposition of Two-Dimensional Transition Metal Dichalcogenides. *Chem. Mater.* **2021**, *33* (18), 7301−7308.

(21) Jiang, D.; Tang, Y.-N.; Wang, D.; Xu, X.; Sun, J.; Ma, R.; Li, W.; Han, Z.; Liu, Y.; Wei, D. Self-Anchored Van-Der-Waals Stacking Growth of Transition-Metal Dichalcogenide Nanoplates. *Adv. Mater.* **2024**, *36* (39), 2407586.

(22) Oh, J.; Park, M.; Kang, Y.; Ju, S.-Y. Real-Time Observation for MoS_2 Growth Kinetics and Mechanism Promoted by the Na Droplet. *ACS Nano* **2024**, *18* (29), 19314−19323.

(23) Fei, L.; Lei, S.; Zhang, W.-B.; Lu, W.; Lin, Z.; Lam, C. H.; Chai, Y.; Wang, Y. Direct TEM Observations of Growth Mechanisms of Two-dimensional MoS_2 Flakes. *Nat. Commun.* **2016**, *7* (1), 12206.

(24) Bayer, B. C.; Kaindl, R.; Reza Ahmadpour Monazam, M.; Susi, T.; Kotakoski, J.; Gupta, T.; Eder, D.; Waldhauser, W.; Meyer, J. C. Atomic-Scale in Situ Observations of Crystallization and Restructuring Processes in Two-Dimensional MoS_2 Films. *ACS Nano* **2018**, *12* (8), 8758−8769.

(25) Leonyuk, N. I.; Pashkova, A. V.; Gokhman, L. Z. Volatility of Potassium Trimolybdate Melt and Solubility of Yttrium-aluminium Borate in It. *J. Cryst. Growth* **1980**, *49* (1), 141−144.

(26) Leonyuk, N. I.; Pashkova, A. V.; Belov, N. V. Neodymium Incorporation into YAl-borate Crystals in Preparation from Solutions in Molten Potassium Trimolybdate. *Krist. Tech.* **1979**, *14* (1), 47−50.

(27) Yang, P.; Zou, X.; Zhang, Z.; Hong, M.; Shi, J.; Chen, S.; Shu, J.; Zhao, L.; Jiang, S.; Zhou, X.; Huan, Y.; Xie, C.; Gao, P.; Chen, Q.; Zhang, Q.; Liu, Z.; Zhang, Y. Batch Production of 6-in. Uniform Monolayer Molybdenum Disulfide Catalyzed by Sodium in Glass. *Nat. Commun.* **2018**, *9* (1), 979.

(28) Bugaris, D. E.; zur Loye, H.-C. Materials Discovery by Flux Crystal Growth: Quaternary and Higher Order Oxides. *Angew. Chem., Int. Ed.* **2012**, *51* (16), 3780−3811.

(29) Nalesso, S.; Bussemaker, M. J.; Sear, R. P.; Hodnett, M.; Lee, J. A Review on Possible Mechanisms of Sonocrystallisation in Solution. *Ultrason. Sonochem.* **2019**, *57*, 125−138.

(30) Xu, J.; Ho, D. Modulation of the Reaction Mechanism via S/Mo: A Rational Strategy for Large-Area MoS_2 Growth. *Chem. Mater.* **2021**, *33* (9), 3249−3257.

(31) Chen, W.; Zhao, J.; Zhang, J.; Gu, L.; Yang, Z.; Li, X.; Yu, H.; Zhu, X.; Yang, R.; Shi, D.; Lin, X.; Guo, J.; Bai, X.; Zhang, G. Oxygen-Assisted Chemical Vapor Deposition Growth of Large Single-Crystal and High-Quality Monolayer MoS_2. *J. Am. Chem. Soc.* **2015**, *137* (50), 15632−15635.

(32) Chen, J.; Tang, W.; Tian, B.; Liu, B.; Zhao, X.; Liu, Y.; Ren, T.; Liu, W.; Geng, D.; Jeong, H. Y.; Shin, H. S.; Zhou, W.; Loh, K. P. Chemical Vapor Deposition of High-Quality Large-Sized MoS_2 Crystals on Silicon Dioxide Substrates. *Adv. Sci.* **2016**, *3* (8), 1500033.

(33) Jiang, H.; Zhang, X.; Chen, K.; He, X.; Liu, Y.; Yu, H.; Gao, L.; Hong, M.; Wang, Y.; Zhang, Z.; Zhang, Y. Two-dimensional Czochralski Growth of Single-crystal MoS_2. *Nat. Mater.* **2025**, *24* (2), 188−196.

(34) Qian, S.; Yang, R.; Lan, F.; Xu, Y.; Sun, K.; Zhang, S.; Zhang, Y.; Dong, Z. Growth of Continuous MoS_2 Film with Large Grain Size by Chemical Vapor Deposition. *Mater. Sci. Semicond. Process.* **2019**, *93*, 317−323.

(35) Shi, Y.; Yang, P.; Jiang, S.; Zhang, Z.; Huan, Y.; Xie, C.; Hong, M.; Shi, J.; Zhang, Y. Na-assisted Fast Growth of Large Single-crystal MoS_2 on Sapphire. *Nanotechnology* **2019**, *30* (3), 034002.

(36) Cong, C.; Shang, J.; Wu, X.; Cao, B.; Peimyoo, N.; Qiu, C.; Sun, L.; Yu, T. Synthesis and Optical Properties of Large-Area Single-Crystalline 2D Semiconductor WS_2 Monolayer from Chemical Vapor Deposition. *Adv. Opt. Mater.* **2014**, *2* (2), 131−136.

(37) Chang, M.-C.; Ho, P.-H.; Tseng, M.-F.; Lin, F.-Y.; Hou, C.-H.; Lin, I. K.; Wang, H.; Huang, P.-P.; Chiang, C.-H.; Yang, Y.-C.; Wang, I. T.; Du, H.-Y.; Wen, C.-Y.; Shyue, J.-J.; Chen, C.-W.; Chen, K.-H.; Chiu, P.-W.; Chen, L.-C. Fast Growth of Large-grain and Continuous MoS_2 Films Through a Self-capping Vapor-liquid-solid Method. *Nat. Commun.* **2020**, *11* (1), 3682.

(38) Tu, Z.; Li, G.; Ni, X.; Meng, L.; Bai, S.; Chen, X.; Lou, J.; Qin, Y. Synthesis of Large Monolayer Single Crystal MoS_2 Nanosheets with Uniform Size through a Double-tube Technology. *Appl. Phys. Lett.* **2016**, *109* (22), 223101.

(39) Zhang, X.; Huangfu, L.; Gu, Z.; Xiao, S.; Zhou, J.; Nan, H.; Gu, X.; Ostrikov, K. Controllable Epitaxial Growth of Large-Area MoS_2/WS_2 Vertical Heterostructures by Confined-Space Chemical Vapor Deposition. *Small* **2021**, *17* (18), 2007312.

(40) Yang, X.; Li, Q.; Hu, G.; Wang, Z.; Yang, Z.; Liu, X.; Dong, M.; Pan, C. Controlled Synthesis of High-quality Crystals of Monolayer MoS_2 for Nanoelectronic Device Application. *Sci. China Mater.* **2016**, *59* (3), 182−190.

(41) Senthilkumar, V.; Tam, L. C.; Kim, Y. S.; Sim, Y.; Seong, M.-J.; Jang, J. I. Direct Vapor Phase Growth Process and Robust Photoluminescence Properties of Large Area MoS_2 Layers. *Nano Res.* **2014**, *7* (12), 1759−1768.

(42) Jiang, H.; Li, L.; Wu, Y.; Duan, R.; Yi, K.; Wu, L.; Zhu, C.; Luo, L.; Xu, M.; Zheng, L.; Gan, X.; Zhao, W.; Wang, X.; Liu, Z. Vapor Deposition of Bilayer 3R MoS_2 with Room-Temperature Ferroelectricity. *Adv. Mater.* **2024**, *36* (32), 2400670.

(43) Yu, H.; Huang, L.; Zhou, L.; Peng, Y.; Li, X.; Yin, P.; Zhao, J.; Zhu, M.; Wang, S.; Liu, J.; Du, H.; Tang, J.; Zhang, S.; Zhou, Y.; Lu, N.; Liu, K.; Li, N.; Zhang, G. Eight In. Wafer-Scale Epitaxial Monolayer MoS_2. *Adv. Mater.* **2024**, *36* (30), 2402855.

(44) Mao, J.; He, J.; Io, W. F.; Guo, F.; Wu, Z.; Yang, M.; Hao, J. Strain-Engineered Ferroelectricity in 2H Bilayer MoS_2. *ACS Nano* **2024**, *18* (44), 30360−30367.

(45) Park, W.; Baik, J.; Kim, T.-Y.; Cho, K.; Hong, W.-K.; Shin, H.-J.; Lee, T. Photoelectron Spectroscopic Imaging and Device Applications of Large-Area Patternable Single-Layer MoS_2 Synthesized by Chemical Vapor Deposition. *ACS Nano* **2014**, *8* (5), 4961−4968.

(46) Liu, Q.; He, J.; Xie, J.; Zhang, H.; Wu, H.; Wang, G.; Lu, X.; Yang, Z. Shielding Unfavorable Interaction by Oxygen-mediated Interlayer Chemical Bonding Enables High-capacity and Stable MoS_2 Cathode. *Nano Energy* **2024**, *127*, 109780.

(47) Kim, I. S.; Sangwan, V. K.; Jariwala, D.; Wood, J. D.; Park, S.; Chen, K.-S.; Shi, F.; Ruiz-Zepeda, F.; Ponce, A.; Jose-Yacaman, M.; Dravid, V. P.; Marks, T. J.; Hersam, M. C.; Lauhon, L. J. Influence of Stoichiometry on the Optical and Electrical Properties of Chemical Vapor Deposition Derived MoS_2. *ACS Nano* **2014**, *8* (10), 10551−10558.

(48) Chowdhury, S.; Roy, A.; Liu, C.; Alam, M. H.; Ghosh, R.; Chou, H.; Akinwande, D.; Banerjee, S. K. Two-Step Growth of Uniform Monolayer MoS_2 Nanosheets by Metal−Organic Chemical Vapor Deposition. *ACS Omega* **2021**, *6* (15), 10343−10351.

(49) Zhang, K.; She, Y.; Cai, X.; Zhao, M.; Liu, Z.; Ding, C.; Zhang, L.; Zhou, W.; Ma, J.; Liu, H.; Li, L.-J.; Luo, Z.; Huang, S. Epitaxial substitution of metal iodides for low-temperature growth of two-dimensional metal chalcogenides. *Nat. Nanotechnol.* **2023**, *18* (5), 448−455.

(50) Ming, H.; Luo, Z.-Z.; Chen, Z.; Cui, H.-H.; Zheng, W.; Zou, Z.; Kanatzidis, M. G. Chemical Pressure-Driven Band Convergence and Discordant Atoms Intensify Phonon Scattering Leading to High Thermoelectric Performance in SnTe. *J. Am. Chem. Soc.* **2024**, *146* (41), 28448−28458.

(51) Li, J.; Wang, S.; Li, L.; Wei, Z.; Wang, Q.; Sun, H.; Tian, J.; Guo, Y.; Liu, J.; Yu, H.; Li, N.; Long, G.; Bai, X.; Yang, W.; Yang, R.; Shi, D.; Zhang, G. Chemical Vapor Deposition of 4 Inch Wafer-Scale Monolayer $MoSe_2$. *Small Sci.* **2022**, *2* (11), 2200062.

(52) Li, X.; Zhang, J.; Puretzky, A. A.; Yoshimura, A.; Sang, X.; Cui, Q.; Li, Y.; Liang, L.; Ghosh, A. W.; Zhao, H.; Unocic, R. R.; Meunier, V.; Rouleau, C. M.; Sumpter, B. G.; Geohegan, D. B.; Xiao, K. Isotope-Engineering the Thermal Conductivity of Two-Dimensional MoS_2. *ACS Nano* **2019**, *13* (2), 2481−2489.

(53) Wan, Y.; Li, E.; Yu, Z.; Huang, J.-K.; Li, M.-Y.; Chou, A.-S.; Lee, Y.-T.; Lee, C.-J.; Hsu, H.-C.; Zhan, Q.; Aljarb, A.; Fu, J.-H.; Chiu, S.-P.; Wang, X.; Lin, J.-J.; Chiu, Y.-P.; Chang, W.-H.; Wang, H.; Shi, Y.; Lin, N.; Cheng, Y.; Tung, V.; Li, L.-J. Low-defect-density WS_2 by Hydroxide Vapor Phase Deposition. *Nat. Commun.* **2022**, *13* (1), 4149.

(54) Abidi, I. H.; Giridhar, S. P.; Tollerud, J. O.; Limb, J.; Waqar, M.; Mazumder, A.; Mayes, E. L. H.; Murdoch, B. J.; Xu, C.; Bhoriya, A.; Ranjan, A.; Ahmed, T.; Li, Y.; Davis, J. A.; Bentley, C. L.; Russo, S. P.; Gaspera, E. D.; Walia, S. Oxygen Driven Defect Engineering of Monolayer MoS_2 for Tunable Electronic, Optoelectronic, and Electrochemical Devices. *Adv. Funct. Mater.* **2024**, *34* (37), 2402402.

(55) Huang, H.; Zha, J.; Xu, S.; Yang, P.; Xia, Y.; Wang, H.; Dong, D.; Zheng, L.; Yao, Y.; Zhang, Y.; Chen, Y.; Ho, J. C.; Chan, H. P.; Zhao, C.; Tan, C. Precursor-Confined Chemical Vapor Deposition of 2D Single-Crystalline Se_xTe_{1-x} Nanosheets for p-Type Transistors and Inverters. *ACS Nano* **2024**, *18* (26), 17293−17303.

(56) Shree, S.; George, A.; Lehnert, T.; Neumann, C.; Benelajla, M.; Robert, C.; Marie, X.; Watanabe, K.; Taniguchi, T.; Kaiser, U.; Urbaszek, B.; Turchanin, A. High Optical Quality of MoS_2 Monolayers Grown by Chemical Vapor Deposition. *2D Mater.* **2020**, *7* (1), 015011.

(57) Tao, L.; Chen, K.; Chen, Z.; Chen, W.; Gui, X.; Chen, H.; Li, X.; Xu, J.-B. Centimeter-Scale CVD Growth of Highly Crystalline Single-Layer MoS_2 Film with Spatial Homogeneity and the Visualization of Grain Boundaries. *ACS Appl. Mater. Interfaces* **2017**, *9* (13), 12073−12081.

(58) Suleman, M.; Lee, S.; Kim, M.; Nguyen, V. H.; Riaz, M.; Nasir, N.; Kumar, S.; Park, H. M.; Jung, J.; Seo, Y. NaCl-Assisted Temperature-Dependent Controllable Growth of Large-Area MoS_2 Crystals Using Confined-Space CVD. *ACS Omega* **2022**, *7* (34), 30074−30086.

(59) Jung, Y.; Ryu, H.; Kim, H.; Moon, D.; Joo, J.; Hong, S. C.; Kim, J.; Lee, G.-H. Nucleation and Growth of Monolayer MoS_2 at Multisteps of MoO_2 Crystals by Sulfurization. *ACS Nano* **2023**, *17* (8), 7865−7871.

(60) Liu, H.; Lin, M.; Guo, S. Morphological and Structural Evolutions of α-MoO_3 Single Crystal Belts towards MoS_2/MoO_2 Heterostructures Upon Post-growth Thermal Vapor Sulfurization. *Appl. Surf. Sci.* **2021**, *536*, 147956.

(61) Li, B.; Gong, Y.; Hu, Z.; Brunetto, G.; Yang, Y.; Ye, G.; Zhang, Z.; Lei, S.; Jin, Z.; Bianco, E.; Zhang, X.; Wang, W.; Lou, J.; Galvão, D. S.; Tang, M.; Yakobson, B. I.; Vajtai, R.; Ajayan, P. M. Solid−Vapor Reaction Growth of Transition-Metal Dichalcogenide Monolayers. *Angew. Chem., Int. Ed.* **2016**, *55* (36), 10656−10661.

(62) Wu, Q.; Fu, X.; Yang, K.; Wu, H.; Liu, L.; Zhang, L.; Tian, Y.; Yin, L.-J.; Huang, W.-Q.; Zhang, W.; Wong, P. K. J.; Zhang, L.; Wee, A. T. S.; Qin, Z. Promoting a Weak Coupling of Monolayer $MoSe_2$ Grown on (100)-Faceted Au Foil. *ACS Nano* **2021**, *15* (3), 4481−4489.

(63) Camacho-López, M. A.; Escobar-Alarcón, L.; Picquart, M.; Arroyo, R.; Córdoba, G.; Haro-Poniatowski, E. Micro-Raman Study of the m-MoO_2 to α-MoO_3 Transformation Induced by Cw-laser Irradiation. *Opt. Mater.* **2011**, *33* (3), 480−484.

(64) Lu, H.-M.; Cao, L.; He, Y.-C.; Yao, S.-H.; Zhou, J.; Lv, Y.-Y.; Chen, Y. B. Growth and Electrical Properties of Polymorphs of Mo-Te Crystals. *Mater. Res. Bull.* **2022**, *151*, 111796.

(65) Huang, S.; Ling, X.; Liang, L.; Kong, J.; Terrones, H.; Meunier, V.; Dresselhaus, M. S. Probing the Interlayer Coupling of Twisted Bilayer MoS_2 Using Photoluminescence Spectroscopy. *Nano Lett.* **2014**, *14* (10), 5500−5508.

(66) Jeon, J.; Jang, S. K.; Jeon, S. M.; Yoo, G.; Jang, Y. H.; Park, J.-H.; Lee, S. Layer-controlled CVD Growth of Large-area Two-dimensional MoS_2 Films. *Nanoscale* **2015**, *7* (5), 1688−1695.

(67) Xia, M.; Li, B.; Yin, K.; Capellini, G.; Niu, G.; Gong, Y.; Zhou, W.; Ajayan, P. M.; Xie, Y.-H. Spectroscopic Signatures of AA′ and AB Stacking of Chemical Vapor Deposited Bilayer MoS_2. *ACS Nano* **2015**, *9* (12), 12246−12254.

(68) Chen, J.; Zhao, X.; Tan, S. J. R.; Xu, H.; Wu, B.; Liu, B.; Fu, D.; Fu, W.; Geng, D.; Liu, Y.; Liu, W.; Tang, W.; Li, L.; Zhou, W.; Sum, T. C.; Loh, K. P. Chemical Vapor Deposition of Large-Size Monolayer $MoSe_2$ Crystals on Molten Glass. *J. Am. Chem. Soc.* **2017**, *139* (3), 1073−1076.

(69) van der Zande, A. M.; Huang, P. Y.; Chenet, D. A.; Berkelbach, T. C.; You, Y.; Lee, G. H.; Heinz, T. F.; Reichman, D. R.; Muller, D. A.; Hone, J. C. Grains and Grain Boundaries in Highly Crystalline Monolayer Molybdenum Disulphide. *Nat. Mater.* **2013**, *12* (6), 554−561.

(70) Wan, X.; Chen, K.; Xie, W.; Wen, J.; Chen, H.; Xu, J.-B. Quantitative Analysis of Scattering Mechanisms in Highly Crystalline CVD MoS_2 through a Self-Limited Growth Strategy by Interface Engineering. *Small* **2016**, *12* (4), 438−445.